International Journal of Nanomedicine

Dovepress
open access to scientific and medical research

Open Access Full Text Article

ORIGINAL RESEARCH

Modified Ce/Zr-MOF Nanoparticles Loaded with Curcumin for Alzheimer's Disease via Multifunctional Modulation

Yan Yang[1,*], Yiling Wang[1,*], Xinran Jiang[1], Jiahao Mi[1], Dizhang Ge[2], Yuna Tong[3], Yuxuan Zhu[1,2]

[1]Department of Pharmacy, Personalized Drug Therapy Key Laboratory of Sichuan Province, Sichuan Academy of Medical Science & Sichuan Provincial People's Hospital, University of Electronic Science and Technology of China, Chengdu, 610072, People's Republic of China; [2]Department of Pharmacy, People's Hospital of Aba Tibetan and Qiang Autonomous Prefecture, Aba, 624000, People's Republic of China; [3]Department of Nephrology, The Third People's Hospital of Chengdu, Chongqing Medical University, Chengdu, 610031, People's Republic of China

*These authors contributed equally to this work

Correspondence: Yuna Tong; Yuxuan Zhu, Email tongyuna1985@163.com; zhuyuxuan6688@163.com

International Journal of Nanomedicine downloaded from https://www.dovepress.com/
For personal use only.

Introduction: Alzheimer's disease (AD), a neurodegenerative condition, stands as the most prevalent form of dementia. Its complex pathological mechanisms and the formidable blood-brain barrier (BBB) pose significant challenges to current treatment approaches. Oxidative stress is recognized as a central factor in AD, underscoring the importance of antioxidative strategies in its treatment. In this study, we developed a novel brain-targeted nanoparticle, Ce/Zr-MOF@Cur-Lf, for AD therapy.

Methods: Layer-by-layer self-assembly technology was used to prepare Ce/Zr-MOF@Cur-Lf. In addition, the effect on the intracellular reactive oxygen species level, the uptake effect by PC12 and bEnd.3 cells and the in vitro BBB permeation effect were investigated. Finally, the mouse AD model was established by intrahippocampal injection of $A\beta_{1\text{-}42}$, and the in vivo biodistribution, AD therapeutic effect and biosafety of the nanoparticles were researched at the animal level.

Results: As anticipated, Ce/Zr-MOF@Cur-Lf demonstrated efficient BBB penetration and uptake by PC12 cells, leading to attenuation of H_2O_2-induced oxidative damage. Moreover, intravenous administration of Ce/Zr-MOF@Cur-Lf resulted in rapid brain access and improvement of various pathological features of AD, including neuronal damage, amyloid-β deposition, dysregulated central cholinergic system, oxidative stress, and neuroinflammation.

Conclusion: Overall, Ce/Zr-MOF@Cur-Lf represents a promising approach for precise brain targeting and multi-target mechanisms in AD therapy, potentially serving as a viable option for future clinical treatment.

Keywords: metal-organic frameworks, Alzheimer's disease, drug delivery, brain targeting, oxidative stress

Introduction

Alzheimer's disease (AD) is a prevalent neurodegenerative disorder characterized by progressive cognitive dysfunction and memory loss.[1] With the aging global population, AD incidence continues to rise. According to the World Alzheimer Report 2022, approximately 55 million people worldwide are currently affected by AD, a number expected to escalate to 139 million by 2050 if no effective interventions are developed.[2] Current treatments only alleviate symptoms and do not cure the disease. This limitation is partly due to the complex and not fully understood mechanisms underlying AD. Notably, two pathological hallmarks of AD are extracellular senile plaques composed of amyloid beta (Aβ) and intracellular neurofibrillary tangles caused by hyperphosphorylated tau protein (pTau).[3,4] Unfortunately, most therapeutic candidates targeting Aβ and pTau have failed to improve cognitive functions in phase II or III clinical trials,[5,6] casting doubt on the long-standing dominance of the Aβ and pTau hypotheses. Consequently, there is a critical need to explore other potential therapeutic targets, such as oxidative stress, to develop more effective treatments for AD.

Recently, the oxidative stress hypothesis has gained attention due to its strong connection with the development of AD. This hypothesis highlights the link between the overproduction of reactive oxygen species (ROS) and AD

Received: 17 July 2024
Accepted: 23 September 2024
Published: 26 September 2024

© 2024 Yang et al. This work is published and licensed by Dove Medical Press Limited. The full terms of this license are available at https://www.dovepress.com/terms.php and incorporate the Creative Commons Attribution – Non Commercial (unported, v3.0) License (http://creativecommons.org/licenses/by-nc/3.0/). By accessing the work you hereby accept the Terms. Non-commercial uses of the work are permitted without any further permission from Dove Medical Press Limited, provided the work is properly attributed. For permission for commercial use of this work, please see paragraphs 4.2 and 5 of our Terms (https://www.dovepress.com/terms.php).

progression.[7] Key sources of ROS in AD include damaged mitochondria,[8] abnormal metal homeostasis,[9] and activated microglia.[10] The gradual accumulation of ROS leads to sustained oxidative stress, a common physiological change in the early stages of AD brains. This stress disrupts the metabolism of biomacromolecules, $Ca^{2+}$and energy homeostasis, mitochondrial function, and synaptic activity, ultimately resulting in cognitive decline.[7] Consequently, oxidative stress is often considered as a core factor in the early phases of AD,[11] potentially preceding other pathological features such as Aβ and tau pathology.[7,12] Moreover, these abnormal metabolisms may further enhance ROS accumulation in a positive feedback loop, creating a vicious cycle that ultimately leads to neuronal death.[4,7] Therefore, therapies targeting excessive ROS could be crucial for effectively treating AD.

Nanozymes, nanomaterials with intrinsic enzyme-like activity, have sparked increasing interest in the redox field due to their stable and desirable enzymatic catalytic functions.[13] Recently, various nanomaterials have been developed to act as artificial nanozymes, mimicking the function of natural antioxidative enzymes. These include Ce-based,[14] palladium,[3] and carbon-based nanoparticles.[15] Among these, Ce-based nanoparticles, particularly ceria nanoparticles, have been reported to effectively regulate oxidative states through a reversible redox ability mediated by Ce ions. The unique redox cycle between Ce^{3+} and Ce^{4+} ions can relieve excess free radicals and mitigate the oxidative stress response of cells under the condition of physiological pH.[16–19] Additionally, mixed-valence ceria exhibited stable antioxidative property, which facilitated to overcome the instability and easy deactivation of natural antioxidants.[20] Thus, mixed-valence ceria were selected for this study to modulate oxidative stress in AD.

Interestingly, nanoparticle-based delivery systems have emerged as an effective strategy to overcome the limitations of therapeutic drugs, including curcumin. Among various nanomaterials, metal-organic frameworks (MOFs) represent a growing class of crystalline porous materials at the nanoscale level. Compared with natural enzymes or catalytic nanomaterials, MOFs have the advantages of high enzyme activity, low cost and good stability, MOFs have garnered extensive interest and are recognized as a potential superior drug delivery materials.[21–23] Specifically, Ce/Zr-MOF is a type of bimetallic mixed metal-organic framework. This compound not only retains the stability of Zr-MOF but also has a smaller size than that of pure Ce-MOF, which is more suitable for in vivo applications.[24] Additionally, Ce/Zr-MOF contains metal Ce ions, which function as ROS scavengers similar to antioxidative enzymes, helping alleviate oxidative stress. Additionally, doping with Zr ions can enhance the catalytic performance of Ce^{3+} and Ce^{4+} states in scavenging ROS.[25–27] Current research on bimetallic Ce/Zr-MOF primarily focuses on its material characteristics, such as structural information,[28] topological transitions,[29] thermal and chemical stability,[24] and detoxification properties against neurotoxic agents.[30] However, few studies have utilized its porous structure to load therapeutic drugs for disease treatment, including AD. In light of this, we have pioneered the use of Ce/Zr-MOF as a nanoplatform for drug delivery and disease treatment.

However, the BBB significantly limits this delivery strategy in the treatment of AD. Consequently, a BBB-targeting unit is essential to ensure precise delivery of the system into the brain. Previous studies have shown that the lactoferrin receptor (LfR) is highly expressed on the surface of cerebrovascular endothelial cells,[31] especially in the brains of those with age-related neurodegenerative diseases such as AD and PD.[32–35] Therefore, LfR-mediated transport across the BBB is considered a promising approach. Concurrently, lactoferrin (Lf) has been widely used as a targeting reagent in the construction of brain-targeted delivery systems.[35,36] By mimicking the endogenous Lf transport route, the Lf-modified nanoplatform can rapidly penetrate the BBB through specific binding with LfR, subsequently exerting intracerebral effects.

Herein, we developed a novel multifunctional nanoparticle, Ce/Zr-MOF@Cur-Lf, with brain targeting ability for AD treatment via multi-pronged modulation (Figure 1). Curcumin was loaded onto a nanoscale bimetallic mixed metal-organic framework (Ce/Zr-MOF) through electrostatic adsorption and coordination interactions. Subsequently, Lf was coated on the surface of Ce/Zr-MOF@Cur to enhance brain targeting, forming Ce/Zr-MOF@Cur-Lf. The coexistence of Ce^{3+} and Ce^{4+} in the MOFs gave it the antioxidative activity to prevent with oxidative stress. Upon intravenous administration, Ce/Zr-MOF@Cur-Lf rapidly accessed the brain via LfR-mediated transport and addressed multiple pathological features of AD mice through a multi-target strategy facilitated by both the carrier and the drug. Moreover, the ROS scavenging ability of Ce/Zr-MOF@Cur-Lf can be further enhanced with the mesoporous structure of MOFs. Overall, our work demonstrates the promising potential of Ce/Zr-MOF@Cur-Lf as a viable candidate for AD therapy.

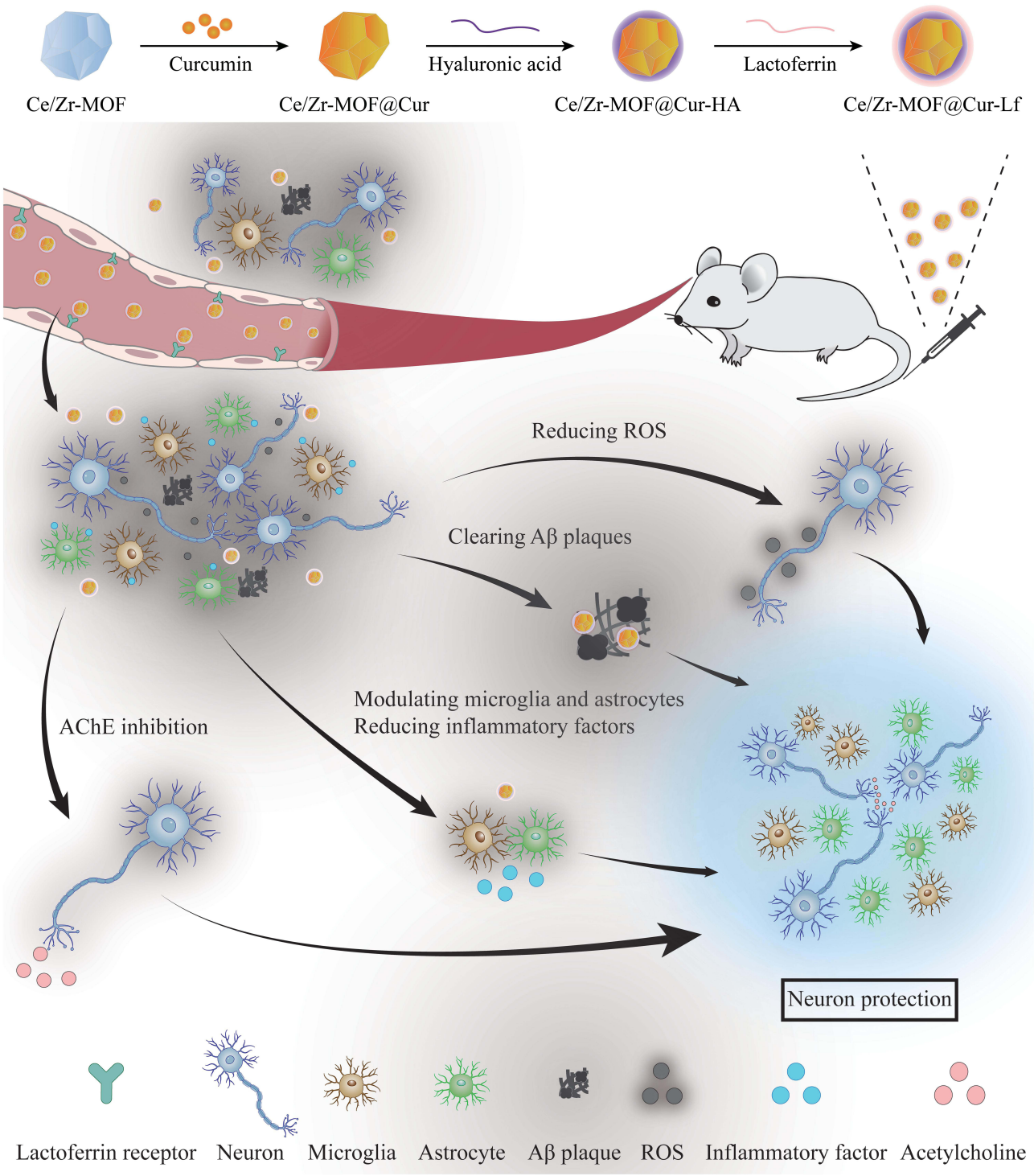

Figure 1 Schematic illustration of the preparation of curcumin-loaded and lactoferrin-modified nanoparticles (Ce/Zr-MOF@Cur-Lf) and the underlying mechanisms for AD therapy after intravenous injection.

Materials and Methods

Materials

We purchased 1.4-phthalic acid (H_2BDC), cerium ammonium nitrate ($NH_4Ce(NO_3)_6$), zirconiumnitrate oxide hydrate ($ZrO(NO_3)_2{\cdot}H_2O$), Lf, hydrogen peroxide (H_2O_2, 3%), and Cur from Shanghai Aladdin Biochemical Technology Co.,

Ltd. (Shanghai, China). Dulbecco's Modified Eagle Medium (DMEM), trypsin, penicillin-streptomycin solution and fetal bovine serum (FBS) were purchased from Hyclone laboratories Inc. (South Logan, UT, USA). Amyloid-β (1–42) protein ($A\beta_{1\text{-}42}$) was purchased from MedCellExpress (New Jersey, USA). RIPA lysis buffer and phenylmethylsulfonyl fluoride (PMSF) were purchased from Beyotime Biotech Inc. (Shanghai, China). All chemical reagents were of analytical grade and pure water was used in all experiments.

Cells

The rat pheochromocytoma PC12 cells and mouse brain microvascular endothelial bEnd.3 cells were provided from the American Type Culture Collection (Rockville, MD, USA). They were cultured in DMEM containing 10% FBS and 1% penicillin-streptomycin solution at 37 °C with 5% CO_2, and the culture medium was changed every 2 days.

Preparation of Ce/Zr-MOF

The synthesis of the mixed-metal Ce/Zr-MOF compound was accomplished following previous synthesis methods with slight modifications.[24,30] Briefly, 127.6 mg of H_2BDC was dissolved in 3.6 mL of DMF and transferred into the reaction bottle. Aqueous solutions of $NH_4Ce(NO_3)_6$ (0.533 M), ($ZrO(NO_3)_2{\cdot}H_2O$ (0.533 M), and 1.03 mL of anhydrous HCOOH were added subsequently. The total volume of the two metal salt solutions was 1200 μL (Table S1). The mixture was then heated at 100 °C for 15 min. Next, the products were first centrifuged at 4000 rpm for 5 min to remove bigger particles. The supernatant was centrifuged at 10000 rpm for 10 min, followed by washing three times with DMF and ethanol. Finally, the products were stored in ethanol at 4 °C.

Preparation of Ce/Zr-MOF@Cur

We added 2.5 mg/mL of Cur ethanol solution into 1 mL of Ce/Zr-MOF ethanol solution. The mixture was continuously stirred for 24 h in the dark at room temperature, then centrifugated and washed three times with ethanol and water, respectively. The obtained precipitation was Ce/Zr-MOF@Cur. The supernatant was collected, in which free Cur was measured using the ultraviolet-visible (UV-vis) method at 433 nm. The drug loading content (LC) and encapsulation efficiency (EE) of Cur were calculated via following equations: LC (%) = (M_0 -M_S)/M*100%; EE (%) = (M_0 -M_S)/M_0*100%. M_0 is the initial mass of curcumin. M_S is the mass of free curcumin in the supernatant. M is total mass of Ce/Zr-MOF@Cur.

Preparation of Ce/Zr-MOF@Cur-Lf

LBL technology was used to prepare the targeted nanoparticles. First, the Ce/Zr-MOF@Cur was coated with negative HA. Different volumes of HA aqueous solution (2 mg/mL) were added into 1 mL of Ce/Zr-MOF@Cur solution. The mixture was mildly stirred for 30 min at room temperature, then centrifugated and washed to obtain Ce/Zr-MOF@Cur-HA. Next, to obtain Lf modified nanoparticles, different volumes of Lf aqueous solution (10 mg/mL) were added to 1 mL of previously prepared Ce/Zr-MOF@Cur-HA. The mixture was gently stirred for 30 min, followed by centrifugation and washing to obtain the final Ce/Zr-MOF@Cur-Lf. The supernatant was collected to determine the content of the free Lf using the BCA Protein Assay kit (Solarbio, PC0020, Beijing, China). The blank Ce/Zr-MOF-Lf was prepared using a similar procedure, with the exception that drugs were added.

Characterization of Nanoparticles

The hydrodynamic diameter (D_H), polydispersity index (PDI), and zeta potential (ZP) were determined by the dynamic light scattering (DLS) method using particle size and a zeta potential analyzer (Litesizer 500, Anton Paar, China). The morphology of nanoparticles was observed via a field-emission scanning electron microscope (SEM, Apreo 2C; Thermo Scientific, USA) and transmission electron microscopy (TEM, Talos F200S; Thermo Scientific, USA). Energy dispersive X-ray spectroscopy (EDS) analysis was performed with an energy dispersive spectrometer (SU8220; Hitachi, Japan). X-ray photoelectron spectroscopy (XPS) was conducted using an X-ray photoelectron spectrometer (ESCALAB Xi^+; Thermo Scientific, USA). X-ray diffraction (XRD) patterns were gained with an X-ray diffractometer (Ultima IV; Rigaku, Japan). An N_2 isothermal adsorption-desorption experiment was performed on an automatic physical adsorption instrument (Autosorb-iQ; Quantachrome, USA). Fourier transform infrared (FTIR) spectroscopy was performed with an

infrared spectrometer (Nicolet Is10; Thermo Scientific, USA). UV-vis absorption spectroscopy was measured via a multifunctional microplate reader (SpectraMax iD5; Molecular, USA).

Release of Cur in vitro

To evaluate the release behavior of Cur in vitro, 1 mg of free Cur dispersed in ethanol solution was used as a control. Ce/Zr-MOF@Cur, Ce/Zr-MOF@Cur-HA, and Ce/Zr-MOF@Cur-Lf containing 1 mg curcumin were loaded in the dialysis bags (30 kDa). The bags were then placed in 15 mL PBS (pH 7.4) solution containing 50% ethanol.[37–39] Then, the devices were shook at 120 rpm and at 37 °C for 5 d. At predetermined time points, an aliquot (5 mL) of dialysis medium was withdrawn, and the same volume of fresh PBS solution was added. The cumulative release rate was calculated via UV-Vis analysis at 433 nm.

Hydroxyl Radical and Superoxide Anion Radical Scavenging Assay

Briefly, 0.5 mL of MV solution (5×10^{-5} M), 0.5 mL of Ce/Zr-MOF or Ce/Zr-MOF-Lf solutions, 0.5 mL $FeSO_4$ solution (5×10^{-3} M) and 0.5 mL H_2O_2 (3%) were added in turn into 0.5 mL of Tris-HCl solution (0.1 M, pH 4.7). After incubation for 5 min at room temperature, the clearance rate at 586 nm was calculated via a multifunctional microplate reader (SpectraMax iD5; Molecular, USA).

0.5 mL of Ce/Zr-MOF or Ce/Zr-MOF-Lf solutions, and 0.1 mL of pyrogallol solution (6 mm) were in turn placed into 5 mL of Tris-HCl solution (0.05 M, pH 8.2). After incubation for 15 min at room temperature, the clearance rate at 318 nm was calculated via a multifunctional microplate reader (SpectraMax iD5; Molecular, USA).

Intracellular ROS Detection

To detect the intracellular ROS level, the 2′,7′-Dichlorofluorescein diacetate (DCFH-DA) probe was used according to the ROS assay kit (Beyotime, S0033S, Shanghai, China). Briefly, PC12 cells were seeded on 24-well plates at a density of 8×10^4 cells/well and cultured overnight. The cells were treated with different drugs for 12 h (H_2O_2, H_2O_2 + Ce/Zr-MOF-Lf, H_2O_2 + free Cur, H_2O_2 + Ce/Zr-MOF@Cur, and H_2O_2 + Ce/Zr-MOF@Cur-Lf). The concentration of curcumin was 2 μg/mL. After co-incubation for 12 h, the culture medium was removed. The cells were washed with PBS, and incubated with DCFH-DA (7.5 μM) for 30 min in the dark. Next, the cells were washed three times with PBS to remove extracellular probes, and observed with an inverted fluorescent microscope (OLYMPUS CKX41, Olympus, Japan). To quantify the results, PC12 cells were collected and resuspended in PBS for a flow cytometry (FCM) analysis (NovoCyte 2070R, Agilent, USA).

Cellular Uptake

The uptake of nanoparticles by PC12 and bEnd.3 cells was evaluated by observing the fluorescent intensity of free FITC and Ce/Zr-MOF-Lf/FITC with a fluorescent microscope. Briefly, PC12 and bEnd.3 cells were seeded on 24-well plates at a density of 8×10^4 cells/well. Free FITC and Ce/Zr-MOF-Lf/FITC at an equal FITC concentration (5, 10, and 20 μg/mL) were added into the plates and incubated for 1, 2, 4, and 6 h. After incubation, the cells were fixed with 4% paraformaldehyde solution for 30 min. Then, the cells were washed and stained with 1 μg/mL DAPI solution for 10 min in the dark. Next, they were washed again and observed using an inverted fluorescent microscope (OLYMPUS CKX41, Olympus, Japan).

In vitro BBB Penetration Assay

To establish the BBB model in vitro, bEnd.3 cells and PC12 cells were employed. Briefly, bEnd.3 cells were seeded in the upper chambers of 12-well Transwell plates (3-μm pore size; JET, China) at a density of 8×10^4 cells/well. Then, PC12 cells were seeded in the lower chambers at a density of 1.5×10^5 cells/well. Free FITC and Ce/Zr-MOF-Lf/FITC at an equal FITC concentration were added into the upper chambers and incubated for 8 h and 12 h, respectively. The cells were collected and resuspended in PBS for FCM analysis (NovoCyte 2070R; Agilent, USA).

In vivo Imaging

We purchased 5-week-old male Balb/c nude (15–18 g) and ICR mice (20–25 g) from Byrness Weil Biotech Ltd. (Sichuan, China) and housed them under a 12/12h dark/light cycle with free access to drinking water and food. All

procedures involving animals were conducted following the ethical guidelines outlined in the Guidelines for Care and Use of experimental animal management committee of Sichuan Provincial People's Hospital, and were approved by the Animal Ethics Committee of Sichuan Provincial People's Hospital. The study was assigned the approval/accreditation number SCXK(CHUAN)2020 − 030.

Male Balb/c nude mice were randomly divided into two groups and injected intravenously with 200 μL of free FITC and Ce/Zr-MOF-Lf/FITC, respectively. At 4, 8, 12, and 24 h after injection, in vivo fluorescent images were collected using an in-vivo imager (AniView100, Biolight, China). The in vivo fluorescent intensity was semi-quantified using AniView software. Next, the mice were immediately euthanized at 24 h post-injection, and different organs (heart, liver, spleen, lungs, kidneys, and brain) were quickly harvested. The ex vivo fluorescence intensity was visualized by an in-vivo imager (AniView100, Biolight, China) and semi-quantitatively analyzed by the AniView software.

Establishment of the AD Model in vivo and Drug Treatment

The AD model was established as described previously.[40,41] The male ICR mice were anesthetized by intraperitoneal injection of 4% chloral hydrate (0.10 mL/10 g) and then fixed in a brain stereotactic apparatus. Each mouse was bilaterally injected into the hippocampus (±1.8 mm lateral, 2.3 mm posterior, 2 mm deep) with 5 μL aggregated $A\beta_{1\text{-}42}$ (1 mg/mL) for 5 min via a microinjection. The needle stayed for another 3 min and was then withdrawn slowly. The sham animals were injected with an equivalent volume of saline.

One week after operation, the mice were randomly divided into six groups (n = 3) for a different treatment. The normal control mice (sham group) were intraperitoneally injected with saline solution every 2 days for seven times. The AD mice (AD group) received $A\beta_{1\text{-}42}$ via a microinjection and were intraperitoneally injected with saline solution every 2 days for seven times. The spare AD mice were treated with different samples (Ce/Zr-MOF-Lf, Cur, Ce/Zr-MOF@Cur and Ce/Zr-MOF@Cur-Lf) every 2 days for seven times (equivalent to 7.5 mg/kg of Cur).

Nissl, HE, Iba-1, and GFAP Immunohistochemistry Staining

The mice were euthanized by cervical dislocation after a 2-week administration. The brain tissues were separated and fixed in 4% paraformaldehyde solution. Then, Nissl staining, HE staining, and immunohistochemistry staining of Iba-1 and GFAP were performed. Both Nissl staining and HE staining were conducted to evaluate the histological change of neurons. Iba-1 and GFAP immunohistochemistry assays were performed to observe the activation status of microglia and astrocytes in the brain, respectively.

Measurement of Hippocampal Indices

To investigate the protective effect of Ce/Zr-MOF@Cur-Lf NPs against AD in vivo, the activity of the antioxidative system and cytokine levels of inflammation in the hippocampus were detected. The hippocampi were separated and homogenized in 1mL of RIPA lysis buffer containing 1 mm PMSF (protease inhibitors), followed by centrifugation at 12500 rpm for 10 min at 4 °C. The supernatant was collected to determine the total protein content using a BCA assay kit (Solarbio, PC0020, Beijing, China). The level of $A\beta_{1\text{-}42}$was detected with an $A\beta_{1\text{-}42}$ ELISA kit (Jianglai, JL11386, Shanghai, China). The AChE activity was determined by an assay kit (Jiancheng, A024-1-1, Nanjing, China). The MDA content and T-SOD activity were quantitatively determined with assay kits (Jiangchen, A003-1-2, A001-1-2, Nanjing, China). Cytokine levels of TNF-α, IL-1β, and IL-6 were quantified with ELISA kits (Neobioscience, EMC102a, EMC001b, EMC004, Shenzhen, China).

Statistical Analysis

All data are presented as the mean ± SD. For multiple-group comparisons, one-way ANOVA was used followed by Tukey's post hoc test. For two-group comparisons, an unpaired Student's *t*-test (two-tailed) was performed. $p < 0.05$ was considered statistically significant (***and *** represent $p< 0.05$, $p< 0.01$, and $p< 0.001$, respectively).

Results and Discussion

Preparation and Characterization of Ce/Zr-MOF

The mixed-metal Ce/Zr-MOF compounds were prepared in one step using the solvothermal method as previously reported.[24,30] As pure Ce-MOF is unstable and easier to form larger aggregates during the synthesis process,[42] Zr ions were chosen as a doping agent to narrow the particle size of the products.[24] It has been reported that the addition of other metal ions, such as Zr,[43] La,[44] and Sm[45] into Ce-based nanoparticles can affect the two states of Ce^{3+} and Ce^{4+}, thereby increasing their catalytic performance in scavenging ROS.[25–27] Based on the results of these previous studies, we synthesized Ce/Zr-MOF. To obtain the ideal Ce/Zr-MOF, the molar ratio of Ce:Zr was optimized using SEM and DLS (Figure 2A and Table S1). First, their morphology and particle size were characterized by SEM. The average diameters of different nanoparticles were 99.35 ± 33.37 nm, 126.54 ± 35.73 nm, and 175.91 ± 56.11 nm, respectively. M01 and M02 were relatively small with uniform dispersion, whereas M03 had a larger particle size, facilitating aggregation. Furthermore, the D_H, PDI, and ZP of products were measured by the DLS method (Figure 2B and Table S2). With the increase of the molar ratio of Ce:Zr, the particle size and PDI gradually increased, which is consistent with the trends of SEM and the results reported in the literature.[24] It should be noted that the slight difference in size between the SEM and DLS results was likely due to the different statuses of nanoparticles during the measurement process, which was

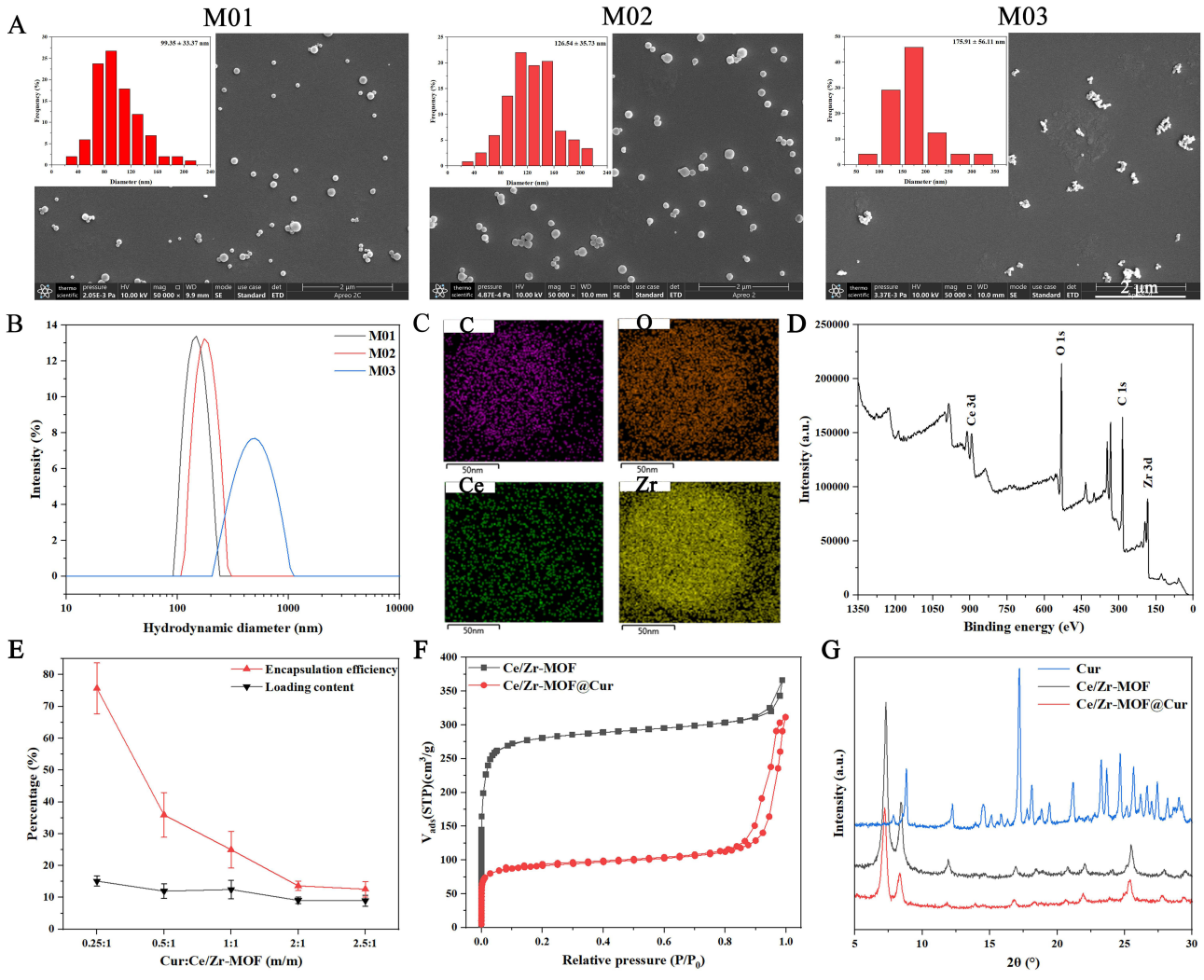

Figure 2 Characterization of Ce/Zr-MOF and Ce/Zr-MOF@Cur. (**A**) SEM images (insert: size distribution) and (**B**) hydrodynamic diameter of Ce/Zr-MOF (M01, M02, and M03). Bar=2 μm. (**C**) EDS mapping images and (**D**) XPS spectra of Ce/Zr-MOF (M02). Bar = 50 nm. (**E**) Loading capacity and encapsulation efficiency of curcumin. The data are presented as mean ± SD (n = 3). (**F**) N_2 absorption-desorption isotherms of Ce/Zr-MOF and Ce/Zr-MOF@Cur. (**G**) XRD patterns of Cur, Ce/Zr-MOF, and Ce/Zr-MOF@Cur.

a normal phenomenon.[46] The ZP of all samples was positive (approximately 43 mV) in water (Table S2), which was helpful for the loading of negative drugs due to electrostatic attraction. Considering that the M01 sample may have contained fewer antioxidant Ce ions, and the M03 sample was unstable, the M02 sample was selected for the subsequent experiments and measurements.

Furthermore, to obtain the elemental distribution and valence states of Ce in the Ce/Zr-MOF, SEM-EDS and XPS were also performed (Figure 2C and Figure S1). The EDS mapping results showed that the nanoparticles contained C, O, Ce, and Zr, whose mass percentages were 37.81%, 24.46%, 1.19%, and 36.54%, respectively, indicating the successful preparation of nanomaterials co-doped with Ce and Zr ions. In addition, the characteristic peaks at 285, 531, 886, and 183 eV in the XPS spectrogram demonstrated the existence of C, O, Ce, and Zr, respectively (Figure 2D), consistent with the EDS results. Notably, the XPS spectrum of Ce 3d suggested that Ce ions in the structure coexisted in the +3 and +4 valence states, and the percentages of the +3 and +4 valence states were 21.74% and 78.26%, respectively (Figure S2). Meanwhile, the peaks at 886.27 and 903.38 eV were attributed to the existence of Ce(III), whereas the peaks at 882.21, 900.61, and 905.45 eV were assigned to the existence of Ce(IV). Previous studies have shown that the larger the ratio of Ce^{3+}/Ce^{4+} in the structure, the better its ability to simulate SOD and perform HORAC for the removal of $O_2^{-}\cdot$ and ·OH, respectively. The smaller the ratio of Ce^{3+}/Ce^{4+}, the better its ability to simulate CAT for the removal of H_2O_2.[17,27] The coexistence of the two valence states allows the Ce ions to exhibit a reversible redox switching between Ce^{3+} and Ce^{4+} to adapt to the ambient chemical environment, which has the ability to scavenge ROS for a prolonged period.[27,47]

Preparation and Characterization of Ce/Zr-MOF@Cur

The LC and EE of Cur in Ce/Zr-MOF was detected via UV-Vis at 433 nm (Figure 2E and Table S3). According to the results, the LC and EE gradually decreased as the weight ratio of Cur: Ce/Zr-MOF increased from 0.25:1 to 2.5:1. When the weight ratio was 0.25:1, the DL and EE were the largest (15.14% ± 1.60% and 75.69% ± 7.99%, respectively). Therefore, the 0.25:1 ratio was chosen as the optimum weight ratio of Cur:Ce/Zr-MOF for loading Cur.

N_2 isothermal adsorption and desorption experiments of Ce/Zr-MOF and Ce/Zr-MOF@Cur were performed (Figure 2F, Figure S3 and Table S4). Ce/Zr-MOF and Ce/Zr-MOF@Cur are both type I isotherms (Langmuir isotherms), which reveals that the Ce/Zr-MOF material is a porous structure. The surface area, micropore volume and micropore diameter of Ce/Zr-MOF@Cur were reduced compared to those of Ce/Zr-MOF, thus confirming the presence of Cur in the Ce/Zr-MOF structure. Furthermore, the crystal structures of Cur, Ce/Zr-MOF, and Ce/Zr-MOF@Cur were characterized by XRD (Figure 2G). The XRD pattern of Ce/Zr-MOF displayed some sharp peaks (7.3°, 8.42°, and 25.5°), indicating crystalline forms of Ce/Zr-MOF.[30] In the diffraction pattern of Ce/Zr-MOF@Cur, the main peaks of Ce/Zr-MOF remained and no new XRD diffraction peak appeared. These results indicate that Cur might be loaded inside the framework, and the structure of Ce/Zr-MOF is stable and not easily affected by drug loading.

Preparation and Characterization of Ce/Zr-MOF@Cur-Lf

LBL technology was used to prepare the Lf modified nanoparticles. This strategy is mainly based on electrostatic adherence between different components. Research has shown that the LBL approach can not only endow the core with a targeting function, but also control the release of cargoes to some extent.[48] HA was chosen as the first layer to provide negative charge due to the positive surface charge of Ce/Zr-MOF@Cur. The morphology of prepared nanoparticles was characterized by TEM (Figure 3A). Ce/Zr-MOF had a small particle size and a slight hexagonal structure. There were very small cavities in the Ce/Zr-MOF microstructure, facilitating drug encapsulation. Compared with Ce/Zr-MOF, the particle size of Ce/Zr-MOF@Cur slightly increased after drug loading, and the internal pores of that decreased. After coating with HA and Lf, a transparent film coating on the outer layer could be observed, especially in blank Ce/Zr-MOF-Lf structures (Figure S4). The particle size and surface potential of prepared particles are measured by the DLS method (Figure 3B, C, and Table S5). The particle size of nanoparticles gradually increased from 201.1nm to 286.0 nm with the increase of the peripheral layers. The low PDI (< 0.25) of all nanoparticles showed good uniformity. The potential of nanoparticles decreased from 41.1 mV to 16.3 mV after loading negative Cur. The potential reversed to −16.0 mV after coating with HA, while after the deposition of the cationic Lf layer, the ZP of NPs became positive (5.2 ± 0.3 mV) again.

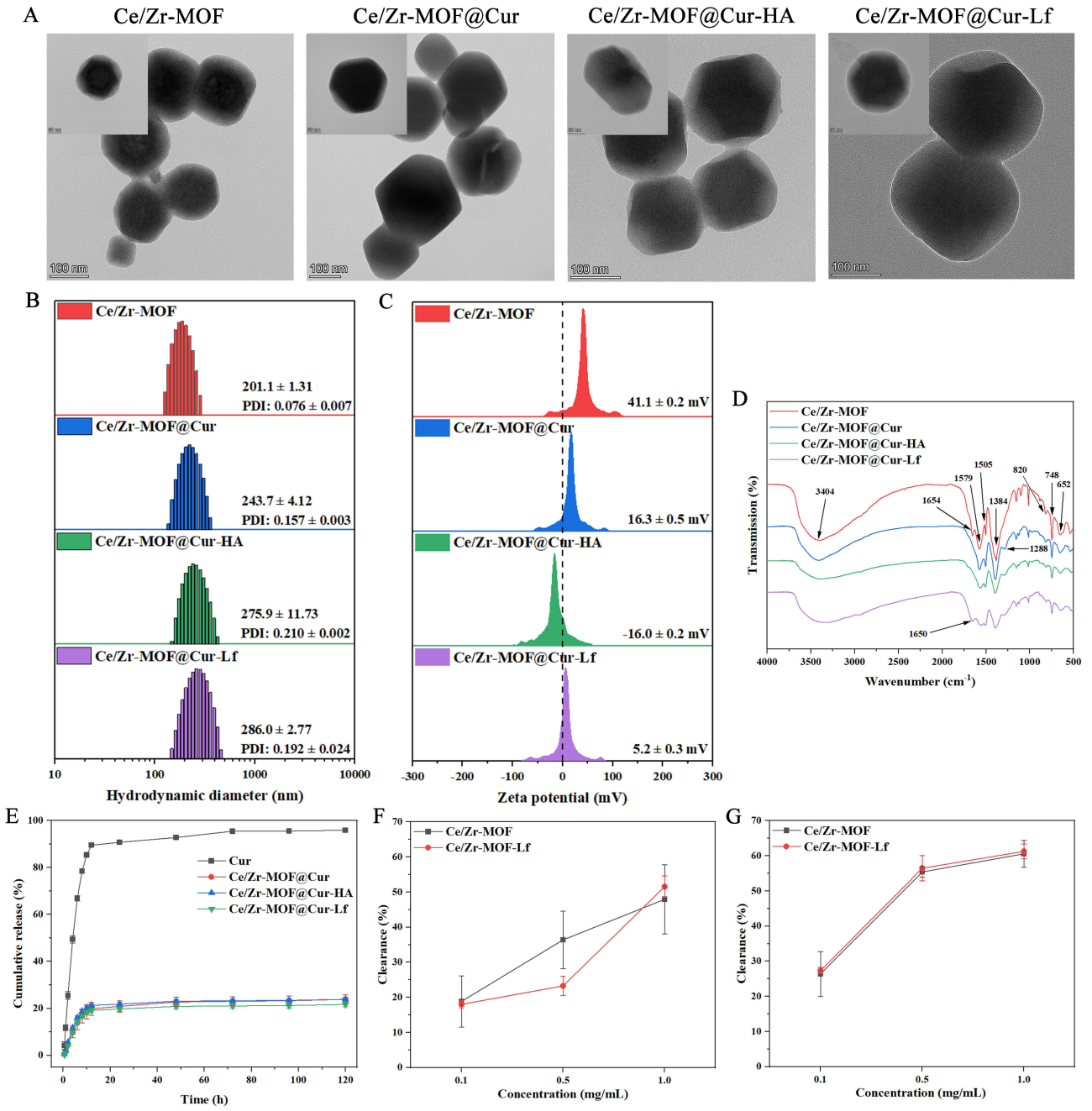

Figure 3 Characterization, drug release, and ROS scavenging performance of nanoparticles. (**A**) TEM images, (**B**) hydrodynamic diameter, (**C**) zeta potential, and (**D**) FTIR spectra of Ce/Zr-MOF, Ce/Zr-MOF@Cur, Ce/Zr-MOF@Cur-HA, and Ce/Zr-MOF@Cur-Lf. Bar =100 nm (inset: bar = 50 nm). (**E**) Cumulative release profile of Cur from different nanoparticles in PBS (pH 7.4). The data are presented as the mean ± SD (n = 3). (**F**) Hydroxyl radical and (**G**) superoxide anion radical clearance rates of Ce/Zr-MOF and Ce/Zr-MOF-Lf under aqueous conditions. The data are presented as mean ± SD (n = 3).

As expected, a complete charge reversal was observed with each coating step, suggesting that the Ce/Zr-MOF@Cur was successfully coated with HA and Lf layers by electrostatic interaction.

The FTIR spectra were obtained to illustrate the chemical structures of the products (Figure 3D). The broad peak 3400 cm^{-1} was considered as the O–H stretching vibration of H_2BDC or H_2O. The weak band at 1654 cm^{-1} was assigned to the C=O carbonyl stretching in H_2BDC,[49] whereas the typical bands at 1579 cm^{-1} and 1384 cm^{-1} were attributed to the O−C−O asymmetric and symmetric stretch in the carboxylate group of H_2BDC.[50] The band located at 1505 cm^{-1} was attributed to the vibration of C=C in the benzene ring. The peaks at 820 cm^{-1}, 748 cm^{-1}, and 652 cm^{-1} could be

attributed to the O−H and C−H vibration of H_2BDC.[51] The spectra of the Ce/Zr-MOF@Cur, Ce/Zr-MOF@Cur-HA, and Ce/Zr-MOF@Cur-Lf were little different from that of Ce/Zr-MOF, indicating that the doping of Cur, HA, and Lf could not affect the chemical structure of Ce/Zr-MOF.

Release of Cur in vitro

The dynamic dialysis method was employed to investigate the in vitro release profile of Cur loaded on preparations (Figure 3E). According to the results, the cumulative release rate of Cur reached 89.50 ± 0.71% within 12 h and 95.47 ± 0.98% within 72 h in the PBS (pH 7.4) solution. However, the cumulative release of Cur from all nanoparticles was only approximately 22% within 72 h, which indicated that nanocarriers could protect Cur from burst release and degradation before targeted cell internalization, showing sustained release behavior.

Intracellular ROS Detection

Excessive ROS in cells can interfere with redox homeostasis and lead to oxidative stress and neuron damage, which is considered an important reason for AD aggravation.[52,53] The clearance rate of Ce/Zr-MOF-Lf increased gradually in a concentration-dependent manner, as detected by the Fenton and pyrogallol reactions (Figure 3F and G). Furthermore, a DCFH-DA probe was used to detect the ROS level in PC12 cells (Figure 4A). After the cells were treated with different drugs, the intracellular ROS fluorescence decreased, especially after the Ce/Zr-MOF@Cur-Lf treatment for 12 h. According to the FCM analysis (Figure 4B), the ROS level significantly decreased after the different drug treatments, which was probably attributed to the ROS scavenging activity mediated by Ce ions in the carrier. Compared with the H_2O_2 group, the Cur and Cur-loaded nano-preparation groups showed a significant reduction in cellular ROS levels, suggesting that Cur has certain antioxidant effects. However, the ROS level in Ce/Zr-MOF@Cur and Ce/Zr-MOF@Cur-Lf groups was lower than that in the free Cur group, which might be due to higher cellular endocytosis and the synergetic antioxidant effects of Cur and Ce ions. These results indicate that Ce/Zr-MOF@Cur-Lf is a potential antioxidant, with potential for use in the treatment of AD-like oxidative stress diseases.

Cellular Uptake

To simulate BBB and neurons in the brain, bEnd.3 and PC12 cells were used, respectively. PC12 and bEnd.3 cells were incubated with both free FITC and FITC-labeled Ce/Zr-MOF-Lf (Ce/Zr-MOF-Lf/FITC) for different durations at 37°C. Cellular uptake was characterized by the fluorescence stain (Figures S5 and S6). The green fluorescence signals gradually increased with the increase of FITC concentration. The results revealed that the cellular accumulation of both FITC and Ce/Zr-MOF-Lf/FITC in PC12 and bEnd.3 cells increased in a concentration-dependent manner. At the same FITC concentration, the green fluorescence signals gradually increased as the incubation time extended (Figures S7 and S8), suggesting that the cellular uptake significantly increased in a time-dependent manner. Moreover, after 6 h of incubation, the uptake amount of Ce/Zr-MOF-Lf/FITC was higher than that of free FITC in PC12 and bEnd.3 cells at the same FITC concentration (Figure 4C–E). The results revealed that Ce/Zr-MOF-Lf could increase the uptake of drugs in PC12 and bEnd.3 cells, which might be attributed to the targeting molecule Lf coated on the surface of the nanoparticles.

In vitro BBB Penetration Assay

To assess the BBB permeation ability of nanoparticles in vitro, a BBB transwell model was established with bEnd.3 cells in the upper chamber and PC12 cells seeded on the lower chamber (Figure 5A). An obvious height difference still observed after 4 h indicates the formation of a dense cell monolayer, successfully establishing an in vitro BBB model (Figure S9). The fluorescence intensity of PC12 cells in the lower chamber after incubation for 8 h and 12 h was measured by FCM (Figure 5B). As the incubation time extended, the fluorescence intensities of FITC and Ce/Zr-MOF-Lf/FITC in PC12 cells gradually intensified, suggesting that the penetration process across the BBB occurred in a time-dependent manner. Moreover, after incubation for 8 h and 12 h, the fluorescence intensity of the Ce/Zr-MOF-Lf/FITC group was stronger than that of the free FITC group, confirming a higher penetration ability of Ce/Zr-MOF-Lf/FITC through the BBB.

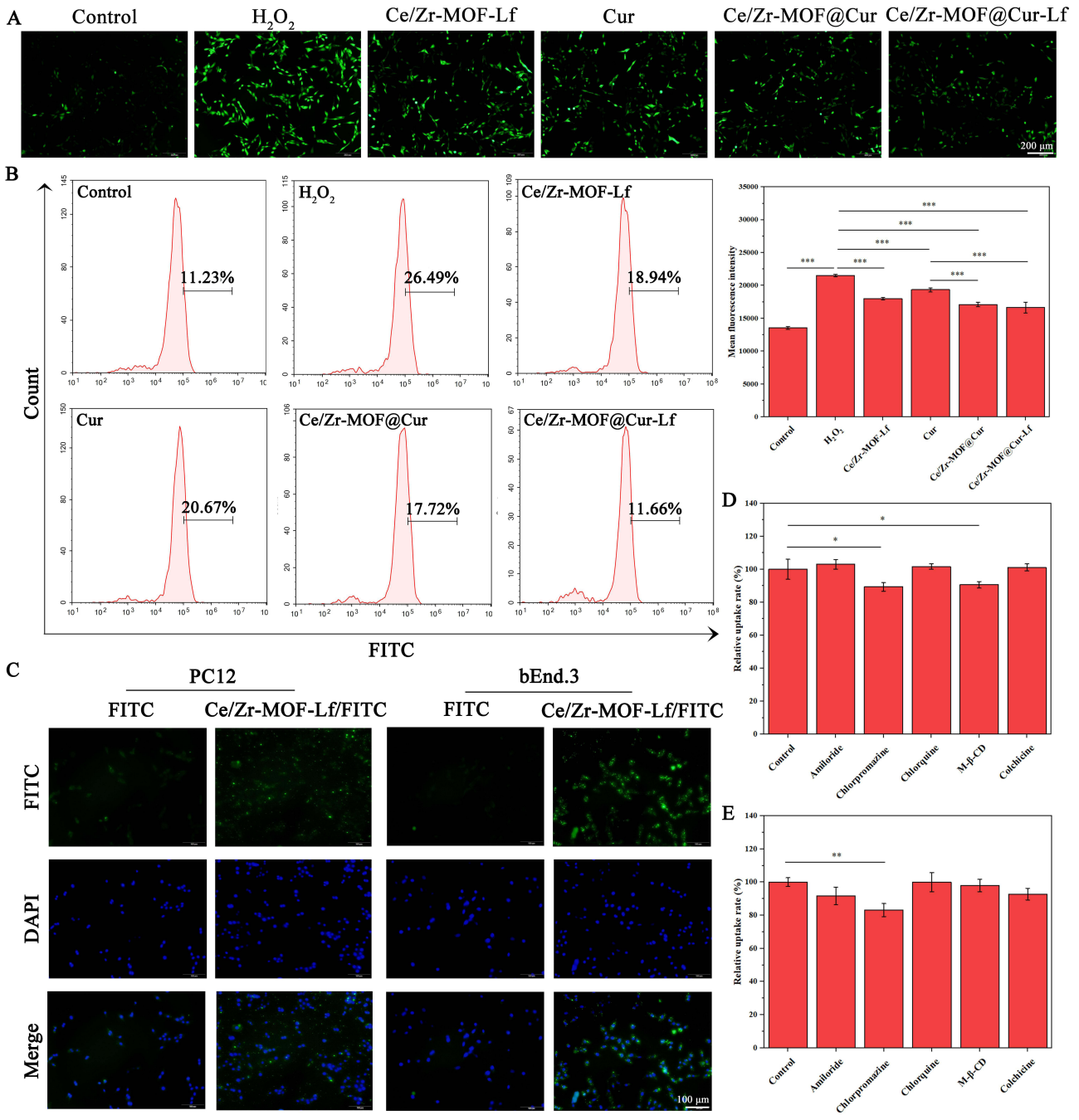

Figure 4 Investigation of intracellular ROS, cellular uptake, and uptake mechanisms. (**A**) Fluorescence images and (**B**) quantitative fluorescence intensity of PC12 cells after different treatments for 12 h, obtained using DCFH-DA. Bar = 200 μm. The data are presented as mean ± SD (n = 3). ***$p < 0.001$. (**C**) Representative uptake images of PC12 and Bend.3 cells after incubation with FITC and Ce/Zr-MOF-Lf/FITC for 6 h. Bar = 100 μm. Relative uptake rates of Ce/Zr-MOF-Lf/FITC in (**D**) PC12 and (**E**) bEnd.3 cells after pretreatment with multiple endocytosis inhibitors. The data are presented as mean ± SD (n = 3). *$p < 0.05$, and **$p < 0.01$.

In vivo Imaging

Motivated by the satisfactory cellular uptake and in vitro BBB penetration performance of Ce/Zr-MOF-Lf/FITC, we further investigated the BBB penetration ability in Balb/c nude mice. FITC and Ce/Zr-MOF-Lf/FITC were intravenously administrated for in vivo tracking. Then, in vivo fluorescence images of FITC were obtained at predesigned time points to monitor their accumulation in the brain and biodistribution in different organs (Figure 5C and D). The fluorescence signal of the Ce/Zr-MOF-Lf/FITC group was stronger in comparison to that of the FITC group in the brain, with the fluorescence signal peaking at 24 h. These results demonstrate enhanced intracerebral accumulation and improved brain-

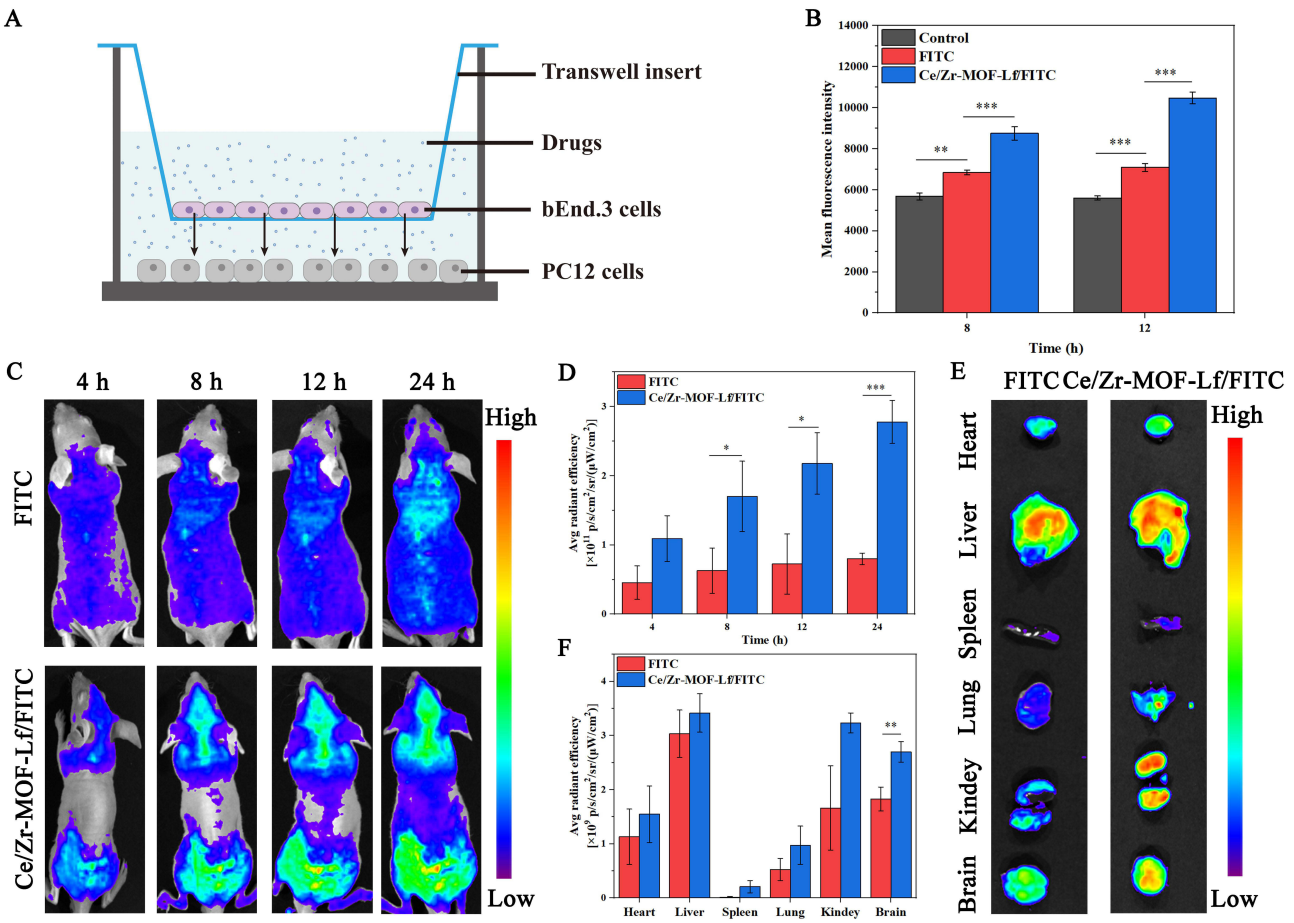

Figure 5 The ability of nanoparticles to penetrate the BBB in vitro and in vivo. (**A**) Schematic illustration of the in vitro BBB transwell model. (**B**) Quantitative fluorescence intensity of PC12 cells after adding FITC and Ce/Zr-MOF-Lf/FITC for 8 h and 12 h. The data are presented as mean ± SD (n = 3). $^{**}p < 0.01$, and $^{***}p < 0.001$. (**C**) In vivo fluorescence imaging of Balb/c nude mice after intravenous injection with FITC and Ce/Zr-MOF-Lf/FITC at different times. (**D**)Semiquantitative analysis of fluorescence intensity in the Balb/c nude mice. The data are presented as mean ± SD (n = 3). $^{*}p < 0.05$, and $^{***}p < 0.001$. (**E**) Ex vivo fluorescence imaging of main organs and brains at 24 h post injection of FITC and Ce/Zr-MOF-Lf/FITC. (**F**) Semiquantitative analysis of fluorescence intensity in different organs. The data are presented as mean ± SD (n = 3). $^{**}p < 0.01$.

targeting capability of Ce/Zr-MOF-Lf/FITC, which might be attributed to the surface exposure of Lf and the enhanced retention effect of nanoparticles.

Next, to further verify the biodistribution of nanoparticles, major organs and brain tissues of Balb/c nude mice were isolated at 24 h post-injection for ex vivo imaging (Figure 5E and F). The weak fluorescence signal of FITC was observed in the brain due to the restriction of BBB. However, the fluorescence intensity of the brain in the Ce/Zr-MOF-Lf/FITC group was 1.48-fold higher than that in the free FITC group, thereby confirming the increasing accumulation of Ce/Zr-MOF-Lf/FITC in the brain. Therefore, the nanoparticles modified with the Lf ligand had the ability to achieve brain targeting, efficiently promoting drug accumulation in the brain, which possibly favors the intracerebral drug availability.

Neuroprotective Effect of Nanoparticles in vivo

To evaluate the neuroprotective performance of Ce/Zr-MOF@Cur-Lf in vivo, Nissl and HE staining were performed (Figure 6A and B). In Nissl staining, darker nuclear staining, nuclear shrinkage, neuronal hypocellularity, and decreasing Nissl bodies are regarded as the pathological characteristics of AD.[54] As we expected, these features could be observed in the cortex and the CA1, CA3, and DG regions of the hippocampus in the $A\beta_{1\text{-}42}$-induced AD group, but not in the sham group. However, the pathological changes could be ameliorated after the treatment, especially using Ce/Zr-MOF@Cur-Lf. A similar phenomenon was also observed after the HE staining of brain sections (Figure 6B). These results demonstrated that Ce/Zr-MOF@Cur-Lf had a protective effect on damaged neurons in AD mice.

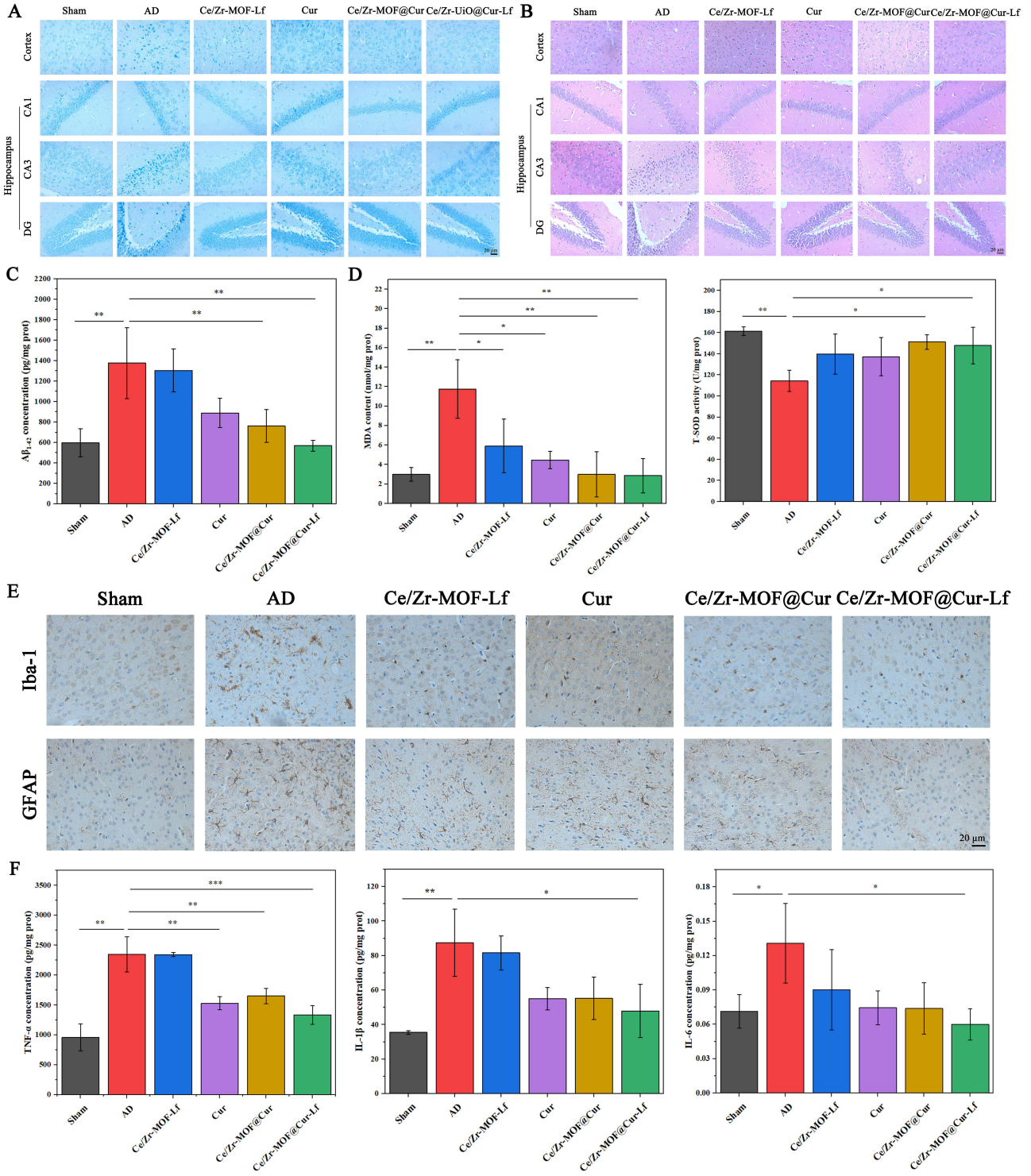

Figure 6 Neuroprotective effect and mechanisms of nanoparticles in AD mice. (**A**) Nissl and (**B**) HE staining in the cortex and hippocampus of mice after treatment with different preparations. Bar = 20 μm. (**C**) Quantitative analysis of $A\beta_{1-42}$ in the hippocampus of mice after treatment with different preparations, determined by an ELISA assay. The data are presented as mean ± SD (n = 3). $^{**}p < 0.01$. (**D**) Quantitative MDA content (left) and T-SOD activity (right) in the hippocampus of mice after treatment with different preparations. The data are presented as mean ± SD (n = 3). $^{*}p < 0.05$, and $^{**}p < 0.01$. (**E**) Iba-1 and GFAP immunohistochemistry staining in the brain of mice after treatment with different preparations. Bar = 20 μm. (**F**) Quantitative analysis of TNF-α (left), IL-1β (middle), and IL-6 (right) in the hippocampus of mice after treatment with different preparations, determined by an ELISA assay. The data are presented as mean ± SD (n = 3). $^{*}p < 0.05$, $^{**}p < 0.01$, and $^{***}p < 0.001$.

https://doi.org/10.2147/IJN.S479242 DovePress

Multiple Mechanisms of Nanoparticles in vivo

To explore the possible mechanisms of nanoparticles for neuroprotective effects, we focused on several key aspects, including Aβ plaques, neuronal acetylcholinesterase (AChE) activity, oxidative stress, and neuroinflammation. The results showed that senile plaques, one of the pathological hallmarks of AD, are caused by Aβ plaque deposition in the brain.[55] Thus, reducing the Aβ burden is considered to be one of the potential strategies in AD therapy. The content of Aβ in the brain of each mice was determined by an ELISA assay (Figure 6C). The results showed that the $A\beta_{1\text{-}42}$ level in the AD group was significantly higher compared to the sham group. Furthermore, the content of $A\beta_{1-42}$ in the brain of AD mice significantly decreased after the Ce/Zr-MOF@Cur and Ce/Zr-MOF@Cur-Lf treatment, suggesting that Ce/Zr-MOF@Cur-Lf has the ability to clear the Aβ plaques in the AD mice.

Additionally, oxidative stress is a contributing factor in the occurrence and development of many neurodegenerative diseases, including AD. Therefore, the MDA content and T-SOD activity in the brain were detected using assay kits (Figure 6D). The MDA content reflects the damage degree to the tissue from ROS, while the T-SOD activity reflects the ability to resist ROS damage. The MDA content in the brain of AD mice was significantly higher, and the T-SOD activity in AD mice was significantly lower than those of sham mice, suggesting that the intrahippocampal injection of $A\beta_{1\text{-}42}$ could facilitate peroxidation, decrease the ability of mice to scavenge free radicals and increase oxidative damage. However, these symptoms were significantly relieved in mice receiving Ce/Zr-MOF@Cur-Lf. Studies have suggested that Cur can downregulate the ROS level and alleviate oxidative damage.[56,57] Furthermore, the Ce ions in the structure of nanoparticles would consume a certain number of ROS, which could further alleviate oxidative stress. Together, these properties enable Ce/Zr-MOF@Cur-Lf to reduce excessive ROS in the brain of AD mice, thus attenuating $A\beta_{1\text{-}42}$-induced oxidative damage.

In addition to high levels of Aβ, abnormal AChE activity, and oxidative stress, neuroinflammation is also a conspicuous brain-threatening factor. A large amount of fuscous Iba-1 microglia staining and GFAP astrocyte staining was found in the brains of AD mice, indicating massive gliosis (Figure 6E). However, fewer activated microglia and astrocytes were observed in AD mice after the treatment with Ce/Zr-MOF@Cur-Lf nanoparticles. Moreover, the expression of TNF-α, IL-1β, and IL-6 in the brain of AD mice was detected using ELISA kits (Figure 6F). The levels of TNF-α, IL-1β, and IL-6 were 2.45-, 2.46-, and 1.83-fold higher, respectively, in the AD mice than those in the sham group. However, the TNF-α, IL-1β, and IL-6 contents decreased significantly after the Ce/Zr-MOF@Cur-Lf treatment, attributed to the anti-inflammatory effects mediated by Cur. These results suggest that Ce/Zr-MOF@Cur-Lf could ameliorate inflammation in the brain by modulating abnormally activated microglia and astrocytes and down-regulating the level of pro-inflammatory cytokines in AD mice. Furthermore, Ce/Zr-MOF@Cur-Lf had excellent biocompatibility and low systemic toxicity (Supplementary Informations 1, 2 and Figure S10), showing great potential in clinical applications.

Conclusion

In summary, novel multifunctional nanoparticles with brain targeting ability and antioxidative properties were constructed for AD treatment. This system has the following merits compared with current AD approaches. (i) Robust antioxidant effect. The +3 and +4 valence states of Ce have been reported to be typically antioxidant, associated with its ROS scavenging ability by mimicking SOD and CAT and performing HORAC. (ii) Multiple target strategies. Ce/Zr-MOF@Cur-Lf has the ability to protect the neurons of AD mice from $A\beta_{1\text{-}42}$-induced damage, down regulate the elevated $A\beta_{1\text{-}42}$ level, balance the cholinergic system, and suppress neuroinflammation. These results may be due to the synergistic effect of carriers and cargoes, displaying promising therapeutic effects in AD model mice. (iii) Excellent brain targeting efficiency. Our system exhibited great BBB penetration ability after connecting with Lf. The nanoparticles have the ability to bypass the BBB and enhance the drug accumulation in mouse brains. Overall, our findings showed that Ce/Zr-MOF@Cur-Lf multifunctional nanoparticles resulted in significant improvements in variable AD pathologies, offering a new choice for AD therapy. Moreover, the antioxidative effect of the Ce/Zr-MOF system may also be applied to the treatment of other oxidative stress-associated diseases.

Acknowledgments

This work was supported by the Research Program of the Science and Technology Department of Sichuan Province [2024YFFK0319]; Research Program of Health Commission of Sichuan Province [21PJ145]; Open Project of Central Nervous System Drug Key Laboratory of Sichuan Province (230015-01SZ); Open Project of Personalized Drug Therapy Key Laboratory of Sichuan Province (2022ZD01), Chengdu Medical College-Sichuan Sansong Medical Management Group Co., Ltd. Joint Research Fund (24LNYXSSB05).

Disclosure

The authors report no conflicts of interest in this work.

References

1. Lu Y, Guo Z, Zhang Y, et al. Microenvironment remodeling micelles for Alzheimer's disease therapy by early modulation of activated microglia. *Adv Sci*. 2019;6(4):1801586. doi:10.1002/advs.201801586
2. Ren Q, Chen H, Chen Y, et al. Imine-linked covalent organic framework modulates oxidative stress in Alzheimer's disease. *ACS Appl Mater Interfaces*. 2023;15(4):4947–4958. doi:10.1021/acsami.2c19839
3. Jia Z, Yuan X, Wei JA, et al. A functionalized octahedral palladium nanozyme as a radical scavenger for ameliorating Alzheimer's disease. *ACS Appl Mater Interfaces*. 2021;13(42):49602–49613. doi:10.1021/acsami.1c06687
4. Cheignon C, Tomas M, Bonnefont-Rousselot D, Faller P, Hureau C, Collin F. Oxidative stress and the amyloid beta peptide in Alzheimer's disease. *Redox Biol*. 2018;14:450–464. doi:10.1016/j.redox.2017.10.014
5. Long JM, Holtzman DM. Alzheimer disease: an update on pathobiology and treatment strategies. *Cell*. 2019;179(2):312–339. doi:10.1016/j.cell.2019.09.001
6. Dam T, Boxer AL, Golbe LI, et al. Safety and efficacy of anti-tau monoclonal antibody gosuranemab in progressive supranuclear palsy: a Phase 2, randomized, placebo-controlled trial. *Nature Med*. 2021;27(8):1451–1457. doi:10.1038/s41591-021-01455-x
7. Tonnies E, Trushina E. Oxidative stress, synaptic dysfunction, and Alzheimer's disease. *J Alzheim Dis*. 2017;57(4):1105–1121. doi:10.3233/JAD-161088
8. Kim TS, Pae CU, Yoon SJ, et al. Decreased plasma antioxidants in patients with Alzheimer's disease. *Internat J Geriat Psych*. 2006;21(4):344–348. doi:10.1002/gps.1469
9. Kozlowski H, Luczkowski M, Remelli M, Valensin D. Copper, zinc and iron in neurodegenerative diseases (Alzheimer's, Parkinson's and prion diseases). *Coord. Chem. Rev.* 2012;256(19–20):2129–2141. doi:10.1016/j.ccr.2012.03.013
10. Nakajima K, Kohsaka S. Microglia: activation and their significance in the central nervous system. *J Biochem*. 2001;130(2):169–175. doi:10.1093/oxfordjournals.jbchem.a002969
11. Hauptmann S, Scherping I, Drose S, et al. Mitochondrial dysfunction: an early event in Alzheimer pathology accumulates with age in AD transgenic mice. *Neurobiol Aging*. 2009;30(10):1574–1586. doi:10.1016/j.neurobiolaging.2007.12.005
12. Uttara B, Singh AV, Zamboni P, Mahajan RT. Oxidative stress and neurodegenerative diseases: a review of upstream and downstream antioxidant therapeutic options. *Curr Neuropharmacol*. 2009;7(1):65–74. doi:10.2174/157015909787602823
13. Yu D, Ma M, Liu Z, et al. MOF-encapsulated nanozyme enhanced siRNA combo: control neural stem cell differentiation and ameliorate cognitive impairments in Alzheimer's disease model. *Biomaterials*. 2020;255:120160. doi:10.1016/j.biomaterials.2020.120160
14. Celardo I, Pedersen JZ, Traversa E, Ghibelli L. Pharmacological potential of cerium oxide nanoparticles. *Nanoscale*. 2011;3(4):1411–1420. doi:10.1039/c0nr00875c
15. Fan K, Xi J, Fan L, et al. In vivo guiding nitrogen-doped carbon nanozyme for tumor catalytic therapy. *Nat Commun*. 2018;9(1):1440. doi:10.1038/s41467-018-03903-8
16. Korsvik C, Patil S, Seal S, Self WT. Superoxide dismutase mimetic properties exhibited by vacancy engineered ceria nanoparticles. *Chem Commun*. 2007;(10):1056–1058. doi:10.1039/b615134e
17. Pirmohamed T, Dowding JM, Singh S, et al. Nanoceria exhibit redox state-dependent catalase mimetic activity. *Chem Commun*. 2010;46(16):2736–2738. doi:10.1039/b922024k
18. Zou S, Zhu X, Zhang L, et al. Biomineralization-inspired synthesis of cerium-doped carbonaceous nanoparticles for highly hydroxyl radical scavenging activity. *Nanoscale Res Lett*. 2018;13(1):76. doi:10.1186/s11671-017-2427-8
19. Das M, Patil S, Bhargava N, et al. Auto-catalytic ceria nanoparticles offer neuroprotection to adult rat spinal cord neurons. *Biomaterials*. 2007;28(10):1918–1925. doi:10.1016/j.biomaterials.2006.11.036
20. Chen Q, Du Y, Zhang K, et al. Tau-targeted multifunctional nanocomposite for combinational therapy of Alzheimer's Disease. *ACS nano*. 2018;12(2):1321–1338. doi:10.1021/acsnano.7b07625
21. Shan J, Du L, Wang X, et al. Ultrasound Trigger Ce-Based MOF nanoenzyme for efficient thrombolytic therapy. *Adv Sci*. 2024;2024:11.
22. Jiang D, Ni D, Rosenkrans ZT, Huang P, Yan X, Cai W. Nanozyme: new horizons for responsive biomedical applications. *Chem Soc Rev*. 2019;2019:48.
23. Yan D, Ling L, Fanggui Y, Shulin Z. A Ce-MOF@polydopamine composite nanozyme as an efficient scavenger for reactive oxygen species and iron in thalassemia disease therapy. *Nanoscale*. 2023;2023:1.
24. Lammert M, Glissmann C, Stock N. Tuning the stability of bimetallic Ce(iv)/Zr(iv)-based MOFs with UiO-66 and MOF-808 structures. *Dalton Trans*. 2017;46(8):2425–2429. doi:10.1039/c7dt00259a
25. Yang Z, Woo TK, Hermansson K. Effects of Zr doping on stoichiometric and reduced ceria: a first-principles study. *J Chem Phys*. 2006;124(22):224704. doi:10.1063/1.2200354

26. Curran CD, Lu L, Jia Y, Kiely CJ, Berger BW, McIntosh S. Direct single-enzyme biomineralization of catalytically active ceria and ceria-zirconia nanocrystals. *ACS nano*. 2017;11(3):3337–3346. doi:10.1021/acsnano.7b00696
27. Soh M, Kang DW, Jeong HG, et al. Ceria-zirconia nanoparticles as an enhanced multi-antioxidant for sepsis treatment. *Angew Chem Int Ed Engl*. 2017;56(38):11399–11403. doi:10.1002/anie.201704904
28. Atzori C, Lomachenko KA, Jacobsen J, et al. Bimetallic hexanuclear clusters in Ce/Zr-UiO-66 MOFs: in situ FTIR spectroscopy and modelling insights. *Dalton Trans*. 2020;49(18):5794–5797. doi:10.1039/d0dt01023e
29. Jacobsen J, Reinsch H, Stock N. Systematic investigations of the transition between framework topologies in Ce/Zr-MOFs. *Inorg Chem*. 2018;57 (20):12820–12826. doi:10.1021/acs.inorgchem.8b02019
30. Geravand E, Farzaneh F, Gil-San-Millan R, Carmona FJ, Navarro JAR. Mixed-metal cerium/zirconium MOFs with improved nerve agent detoxification properties. *Inorg Chem*. 2020;59(22):16160–16167. doi:10.1021/acs.inorgchem.0c01434
31. Liu Z, Jiang M, Kang T, et al. Lactoferrin-modified PEG-co-PCL nanoparticles for enhanced brain delivery of NAP peptide following intranasal administration. *Biomaterials*. 2013;34(15):3870–3881. doi:10.1016/j.biomaterials.2013.02.003
32. An L, Sato H, Konishi Y, et al. Expression and localization of lactotransferrin messenger RNA in the cortex of Alzheimer's disease. *Neurosci Lett*. 2009;452(3):277–280. doi:10.1016/j.neulet.2009.01.071
33. Faucheux BA, Nillesse N, Damier P, et al. Expression of lactoferrin receptors is increased in the mesencephalon of patients with Parkinson disease. *Proc Natl Acad Sci USA*. 1995;92(21):9603–9607. doi:10.1073/pnas.92.21.9603
34. Grau AJ, Willig V, Fogel W, Werle E. Assessment of plasma lactoferrin in Parkinson's disease. *Movem Disord*. 2001;16(1):131–134. doi:10.1002/1531-8257(200101)16:1<131::aid-mds1008>3.0.co;2-o
35. Meng F, Asghar S, Gao S, et al. A novel LDL-mimic nanocarrier for the targeted delivery of curcumin into the brain to treat Alzheimer's disease. *Colloids Surf B Biointerfaces*. 2015;134:88–97. doi:10.1016/j.colsurfb.2015.06.025
36. Lalani J, Raichandani Y, Mathur R, et al. Comparative receptor based brain delivery of tramadol-loaded poly(lactic-co-glycolic acid) nanoparticles. *J Biomed Nanotechnol*. 2012;8(6):918–927. doi:10.1166/jbn.2012.1462
37. Shababdoust A, Zandi M, Ehsani M, Shokrollahi P, Foudazi R. Controlled curcumin release from nanofibers based on amphiphilic-block segmented polyurethanes. *Int J Pharm*. 2020;575:118947. doi:10.1016/j.ijpharm.2019.118947
38. Wang W, Zhu R, Xie Q, et al. Enhanced bioavailability and efficiency of curcumin for the treatment of asthma by its formulation in solid lipid nanoparticles. *Int J Nanomed*. 2012;7:3667–3677. doi:10.2147/IJN.S30428
39. Tiwari SK, Agarwal S, Seth B, et al. Curcumin-loaded nanoparticles potently induce adult neurogenesis and reverse cognitive deficits in Alzheimer's disease model via canonical Wnt/β-catenin pathway. *ACS nano*. 2014;8(1):76–103. doi:10.1021/nn405077y
40. Zheng X, Pang X, Yang P, et al. A hybrid siRNA delivery complex for enhanced brain penetration and precise amyloid plaque targeting in Alzheimer's disease mice. *Acta Biomater*. 2017;49:388–401. doi:10.1016/j.actbio.2016.11.029
41. Huang M, Hu M, Song Q, et al. GM1-modified lipoprotein-like nanoparticle: multifunctional nanoplatform for the combination therapy of Alzheimer's disease. *ACS nano*. 2015;9(11):10801–10816. doi:10.1021/acsnano.5b03124
42. Farrag M. In situ preparation of palladium nanoclusters in cerium metal-organic frameworks Ce-MOF-808, Ce-UiO-66 and Ce-BTC as nanoreactors for room temperature Suzuki cross-coupling reaction. *Microp Mesop Mat*. 2021;312:110783. doi:10.1016/j.micromeso.2020.110783
43. Tsai YY, Oca-Cossio J, Lin SM, Woan K, Yu PC, Sigmund W. Reactive oxygen species scavenging properties of ZrO2-CeO2 solid solution nanoparticles. *Nanomedicine*. 2008;3(5):637–645. doi:10.2217/17435889.3.5.637
44. Fernandez-Garcia S, Jiang L, Tinoco M, et al. Enhanced hydroxyl radical scavenging activity by doping lanthanum in ceria nanocubes. *J Phys Chem C*. 2016;120(3):1891–1901. doi:10.1021/acs.jpcc.5b09495
45. Celardo I, De Nicola M, Mandoli C, Pedersen JZ, Traversa E, Ghibelli L. Ce^{3+} ions determine redox-dependent anti-apoptotic effect of cerium oxide nanoparticles. *ACS nano*. 2011;5(6):4537–4549. doi:10.1021/nn200126a
46. Zhu Q, Fan Z, Zuo W, Chen Y, Hou Z, Zhu X. Self-distinguishing and stimulus-responsive carrier-free theranostic nanoagents for imaging-guided chemo-photothermal therapy in small-cell lung cancer. *ACS Appl Mater Interfaces*. 2020;12(46):51314–51328. doi:10.1021/acsami.0c18273
47. Choi B, Soh M, Manandhar Y, et al. Highly selective microglial uptake of ceria-zirconia nanoparticles for enhanced analgesic treatment of neuropathic pain. *Nanoscale*. 2019;11(41):19437–19447. doi:10.1039/c9nr02648g
48. Kabary DM, Helmy MW, Elkhodairy KA, Fang JY, Elzoghby AO. Hyaluronate/lactoferrin layer-by-layer-coated lipid nanocarriers for targeted co-delivery of rapamycin and berberine to lung carcinoma. *Colloids Surf B Biointerfaces*. 2018;169:183–194. doi:10.1016/j.colsurfb.2018.05.008
49. Ebrahim AM, Bandosz TJ. Ce(III) doped Zr-based MOFs as excellent NO2 adsorbents at ambient conditions. *ACS Appl Mater Interfaces*. 2013;5 (21):10565–10573. doi:10.1021/am402305u
50. Ning H, Yang Z, Yin Z, et al. A novel strategy to enhance the performance of CO2 adsorption separation: grafting hyper-cross-linked polyimide onto composites of UiO-66-NH2 and GO. *ACS Appl Mater Interfaces*. 2021;13(15):17781–17790. doi:10.1021/acsami.1c00917
51. Fan Y, Zhang H, Ren M, et al. Low-temperature catalytic degradation of chlorinated aromatic hydrocarbons over bimetallic Ce-Zr/UiO-66 catalysts. *Chem Eng J*. 2021;414:128782. doi:10.1016/j.cej.2021.128782
52. Dalle-Donne I, Aldini G, Carini M, Colombo R, Rossi R, Milzani A. Protein carbonylation, cellular dysfunction, and disease progression. *J Cell & Mol Med*. 2006;10(2):389–406. doi:10.1111/j.1582-4934.2006.tb00407.x
53. Perry G, Castellani RJ, Hirai K, Smith MA. Reactive oxygen species mediate cellular damage in Alzheimer disease. *J Alzheim Dis*. 1998;1 (1):45–55. doi:10.3233/jad-1998-1103
54. Yang X, Yang W, Xia X, et al. Intranasal Delivery of BACE1 siRNA and rapamycin by dual targets modified nanoparticles for Alzheimer's disease therapy. *Small*. 2022;18(30):e2203182. doi:10.1002/smll.202203182
55. Tiwari S, Atluri V, Kaushik A, Yndart A, Nair M. Alzheimer's disease: pathogenesis, diagnostics, and therapeutics. *Int J Nanomed*. 2019;14:5541–5554. doi:10.2147/ijn.S200490
56. Ak T, Gülçin I. Antioxidant and radical scavenging properties of curcumin. *Chem. Biol. Interact.* 2008;174(1):27–37. doi:10.1016/j.cbi.2008.05.003
57. Gibellini L, Bianchini E, De Biasi S, Nasi M, Cossarizza A, Pinti M. Natural compounds modulating mitochondrial functions. *Evid Based Complement Alternat Med*. 2015;2015:527209. doi:10.1155/2015/527209

International Journal of Nanomedicine Dovepress

Publish your work in this journal

The International Journal of Nanomedicine is an international, peer-reviewed journal focusing on the application of nanotechnology in diagnostics, therapeutics, and drug delivery systems throughout the biomedical field. This journal is indexed on PubMed Central, MedLine, CAS, SciSearch®, Current Contents®/Clinical Medicine, Journal Citation Reports/Science Edition, EMBase, Scopus and the Elsevier Bibliographic databases. The manuscript management system is completely online and includes a very quick and fair peer-review system, which is all easy to use. Visit http://www.dovepress.com/testimonials.php to read real quotes from published authors.

Submit your manuscript here: https://www.dovepress.com/international-journal-of-nanomedicine-journal